# SeaQuaKE: Sea-optimized Quantum Key Exchange

## Final Report

Prepared for: Office of Naval Research
Contract #: N00014-14-C-0003
January 2015

_____

**Prepared by:**

Paul Toliver
732-898-8146
ptoliver@appcomsci.com

James M. Dailey
732-898-8054
jdailey@appcomsci.com

## Applied Communication Sciences

*Drawing on its Telcordia, Bellcore and Bell Labs heritage, Applied Communication Sciences excels at creating innovative technologies and services to solve the most difficult and complex information and communications problems across commercial, carrier and government sectors. Applied Communication Sciences is legally registered as Vencore Labs, Inc., doing business as Applied Communication Sciences. ACS operates as a standalone company under the corporate umbrella of its owner, Vencore, Inc.*

# REPORT DOCUMENTATION PAGE

FORM APPROVED
OMB No. 0704-0188

Public reporting burden for this collection of information is estimated to average 1 hour per response, including the time for reviewing instructions, searching existing data sources, gathering and maintaining the data needed, and completing and reviewing the collection of information. Send comments regarding this burden estimate or any other aspect of this collection of information, including suggestions for reducing this burden to Department of Defense, Washington Headquarters Services. Directorate for Information Operations and Reports (0704-0188), 1215 Jefferson Davis Highway, Suite 1204 Arlington, VA 22202-4302. Respondents should be aware that notwithstanding any other provision of law, no person shall be subject to any penalty for failing to comply with a collection of information if it does not display a currently valid OMB control number. **PLEASE DO NOT RETURN YOUR FORM TO THE ABOVE ADDRESS.**

| 1. REPORT DATE | 2. REPORT TYPE | 3. DATES COVERED *(From - To)* |
|---|---|---|
| January 2015 | Final Report | February 2014 − January 2015 |

**4. TITLE AND SUBTITLE**

SeaQuaKE: Sea-optimized Quantum Key Exchange

Final Report

**5a. CONTRACT NUMBER**
N00014-14-C-0003

**5b. GRANT NUMBER**

**5c. PROGRAM ELEMENT NUMBER**

**6. AUTHOR(S)**

Paul Toliver and James M. Dailey

**5d. PROJECT NUMBER**

**5e. TASK NUMBER**

**5f. WORK UNIT NUMBER**

**7. PERFORMING ORGANIZATION NAME(S) AND ADDRESS(ES)**

Vencore Labs Inc. (dba Applied Communication Sciences)
150 Mount Airy Road
Basking Ridge, NJ 07920-2021

**8. PERFORMING ORGANIZATION REPORT NUMBER**

**9. SPONSORING/MONITORING AGENCY NAME(S) AND ADDRESS(ES)**

Office of Naval Research
875 North Randolph Street, Arlington VA 22203

DCMA Springfield
Bldg. 93, Picatinny Arsenal, NJ 07806-5000

**10. SPONSOR/MONITOR'S ACRONYM(S)**
ONR, DCMA

**11. SPONSOR/MONITOR'S REPORT NUMBER(S)**

**12. DISTRIBUTION/AVAILABILITY STATEMENT**

Distribution Statement A. Approved for public release; distribution is unlimited

**13. SUPPLEMENTARY NOTES**

**14. ABSTRACT**

This is the Final Report summarizing progress on the Sea-optimized Quantum Key Exchange (SeaQuaKE) project, which is led by Applied Communications Sciences under the ONR Free Space Optical Quantum Key Distribution Special Notice (13-SN-0004 under ONRBAA13-001).

In this report, we summarize the results of our 1-year effort to assess critical wavelength-dependent performance considerations of a free-space, maritime quantum communication system utilizing hyperentangled states. Important aspects of the quantum transmitter, quantum channel, and quantum receiver elements are included in our end-to-end systems model. The system performance at a number of infrared transmission windows, ranging from near- to long-wavelength-infrared, was projected under different atmospheric conditions. The results were used to highlight potential operating regions within this broad infrared spectrum where the highest performance of such systems might be achievable.

**15. SUBJECT TERMS**

Quantum communications, free-space optical communications

| 16. SECURITY CLASSIFICATION OF: | | | 17. LIMITATION OF ABSTRACT | 17. NUMBER OF PAGES | 19. NAME OF RESPONSIBLE PERSON |
|---|---|---|---|---|---|
| **a. REPORT** | **b. ABSTRACT** | **c. THIS PAGE** | Same as report (SAR) | 25 | **20. TELEPHONE NUMBER** |
| Unclassified | Unclassified | Unclassified | | | |

Standard Form 298 (Rev. 8--98)
Prescribed by ANSI Std. Z39.18

# Table of Contents

# 1   Summary

This is the Final Report summarizing progress on the Sea-optimized Quantum Key Exchange (SeaQuaKE) project, which is led by Applied Communications Sciences under the ONR Free Space Optical Quantum Key Distribution Special Notice (13-SN-0004 under ONRBAA13-001).

In this report, we summarize the results of our 1-year effort to assess critical wavelength-dependent performance considerations of a free-space, maritime quantum communications system utilizing hyperentangled states. Important aspects of the quantum transmitter, quantum channel, and quantum receiver elements are included in our end-to-end systems model. The system performance at a number of infrared transmission windows, ranging from near- to long-wavelength-infrared, was projected under different atmospheric conditions. The results were used to highlight potential operating regions within this broad infrared spectrum where the highest performance of such systems might be achievable.

# 2    Introduction

The objective of the ONR SeaQuaKE project is to optimize the performance of free-space optical (FSO) quantum key distribution (QKD) operating under challenging maritime atmospheric conditions. In particular, a modeling framework was developed to help guide optimization of the *system operating wavelength* in order to maximize throughput and/or transmission distance over a range of atmospheric conditions. The framework takes an end-to-end system modeling approach by considering each of the major components of a quantum communication system including the quantum transmitter, quantum channel, and quantum receiver elements. During this project, Applied Communication Sciences (ACS) has focused its efforts on the quantum transmitter and receiver elements, while Stevens Institute of Technology (SIT) focused their efforts on the free-space quantum channel.

During our SeaQuaKE project, which was limited to 1 year in duration, ACS efforts on the quantum transmitter element were focused on developing a hyperentanglement-based source architecture that could allow for operation at a particular wavelength that might lie anywhere from the near infrared to far infrared region (from ~0.8 μm to more than 10 μm). In addition, a detailed source model was developed to project the performance that might be achievable from such a source given realistic wavelength-dependent component and material characteristics.

As part of the quantum channel effort, SIT utilized the MODTRAN simulation environment [1] to estimate the wavelength dependencies of free-space transmission under a range of atmospheric and visibility conditions. Similar to the transmitter element, a broad range of wavelengths (from ~0.8 μm to 10 μm) were considered in the free-space channel analysis.

Most recently, as part of the last quarter of the project, ACS developed and analyzed a superconducting nanowire single-photon detector (SNSPD) model for use within the quantum receiver element. This new detector model goes beyond the empirical model we had been using previously, which only projected wavelength dependent detection efficiencies based upon SNSPDs that had been demonstrated to date. The latest SNSPD model is used to project the wavelength-dependant limits of performance that might be possible given appropriate fabrication technologies.

The models for all three elements, including the quantum transmitter, channel, and receiver, were all combined in order to project the end-to-end system performance of a quantum communications system under different atmospheric conditions. Of particular interest are the regions of operating wavelength where system models predict the best expected performance.

# 3 Methods, Assumptions and Procedures

## 3.1 System Overview

As part of this effort, we have focused on the key physical-layer considerations of a hyperentanglement-based quantum communications system, which is illustrated as a block diagram in Figure 1 below. Within the *quantum transmitter* element, we have assumed the use of hyperentanglement–based encoding techniques [2], which double the entangled bits (ebits) that can be carried by allowing for entanglement of photon pairs in both polarization [3] and time-bin [4] degrees of freedom simultaneously. Entanglement analysis components in both the polarization and time domain are used at both the transmit and receive end (i.e. within the *quantum receiver* element) for state measurements by single-photon detectors. These measurement results can then be used in combination with quantum communication protocols, such as quantum key distribution (QKD).

In the link between the transmitter and receiver elements lies the free-space quantum channel. The key considerations of the channel, particularly when one considers the very low signal power present in a typical quantum communication system, include the following: (i) loss from atmospheric absorption and scattering, (ii) introduction of additional background noise from sources such as blackbody radiation, and (iii) beam impairments from inhomogeneities in the path, such as atmospheric turbulence.
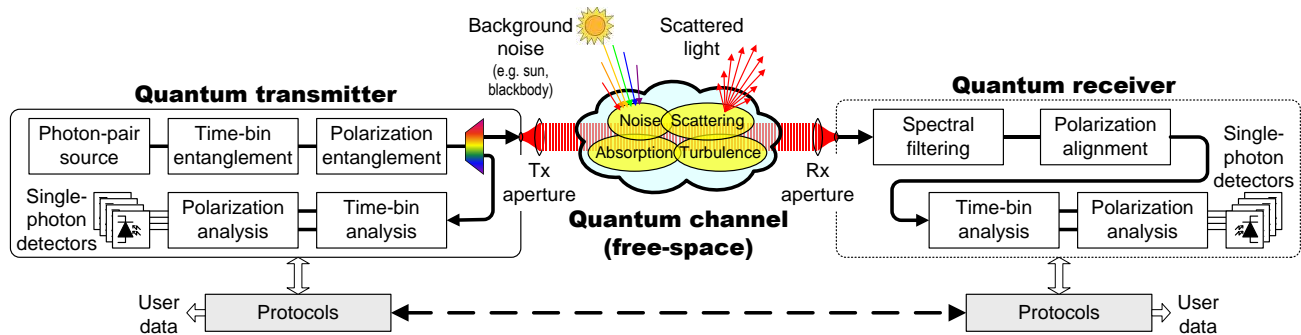


Figure 1. Block diagram of quantum communications system and major physical layer elements considered, including the quantum transmitter, quantum channel, and quantum receiver elements.

Optimizing such a system by minimizing total loss and minimizing impairments is critical to delivering overall system goals such as long transmission link distances and high quantum communications throughput. Since the wavelength at which such a system operates can have a dramatic impact on performance, the focus of this project has been to explore to what degree it can be optimized given particular atmospheric conditions and realistic technology constraints. The major bands of interest considered here and the approximate wavelength ranges assumed include the following: near infrared (NIR ~0.75-1.4 μm), short-wavelength infrared (SWIR ~1.4-3 μm), mid-wave infrared (MWIR ~3-8 μm), and long-wavelength infrared (LWIR ~8-15 μm).

## 3.2 Quantum Transmitter: Source Architecture and Modeling

As mentioned briefly in the previous section, we are assuming the use of a hyperentanglement-based source to serve as the primary transmitter element of a maritime quantum communications system. Such a source allows for entanglement in multiple degrees of freedom, resulting in potentially greater throughput per entangled photon pair compared to alternative sources that encode in only a

single degree of freedom. In addition, the use of entanglement-based system versus a prepare-and-measure quantum communications approach can simplify the need for high-speed random number generation. The two degrees of freedom we will focus on in our study include polarization and time-bin, both of which can be carried, at least in principle, within a single spatial mode of an optical fiber or waveguide. Higher-order spatial modes (e.g. orbital angular momentum), on the other hand, will not be considered here, due to the challenges that harsh atmospheric propagation environments can present for such signals [5].

The focus of our source effort is to understand the critical components and key performance parameters that vary *as a function of system operating wavelength*. As shown in Figure 2 below, the hyperentanglement source can be broken down further into three smaller subsystems, including the pump source, time-bin multiplexer, polarization entanglement & pair generation elements. Also shown are some of the technology considerations and relevant parameters in each of these subsystems.

At the heart of this entanglement source is a relatively high-power pulsed pump along with a passive optical fiber medium that generates correlated photon pairs non-deterministically through the process of spontaneous four-wave mixing (SFWM). These two elements are combined with additional passive optical components that prepare entangled states in both time and polarization degrees of freedom.
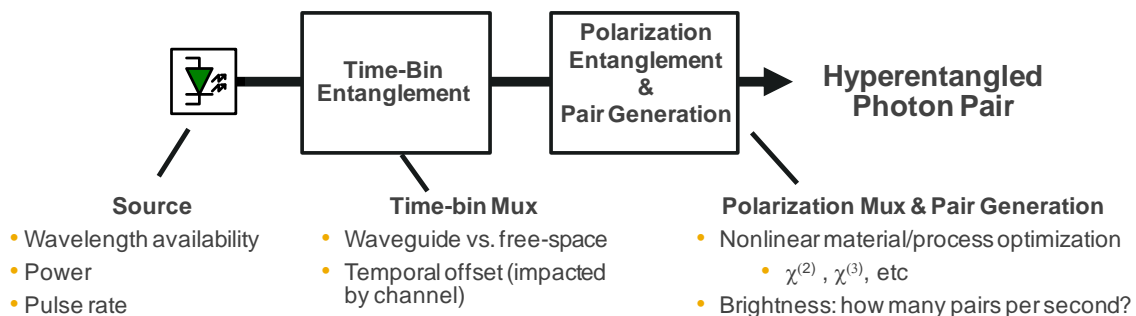


Figure 2: Block diagram of a hyperentanglement source with time-bin and polarization degrees of freedom

The approach we took initially in the development of a hyperentanglement source model was to survey the current body of literature on this topic to understand architectural options, state-of-the-art performance capabilities, trends towards improved performance, as well as fundamentals limits of specific enabling technologies. In particular, it was critically important to understand how each of these factors varied as a function of source operating wavelength. As discussed in more detail in the remainder of this report, we've focused our modeling studies on five particular infrared wavelength bands with the highest likelihood to provide reasonably good atmospheric transmission windows: 0.8, 1.3, 1.5, 3.5, 5, and 9 μm. Ultimately, the various parameters for materials and components forming the source translate to a range of higher-level source metrics that we've considered as part of our study, including the following:

- Entanglement quality
- Pair probability
- Pump repetition frequency
- Signal-to-noise
- Mode quality

We considered a range of available material technologies for the correlated photon pair generation and chose materials representing state-of-the-art, including those currently being considered for nonlinear optics work in the NIR and MWIR bands. Our survey of pump technology concluded that sources at each wavelength of interest were feasible for generating sufficient peak powers to optimally utilize the selected materials. We developed a source model using nonlinear optics SFWM equations, which allows us to calculate correlated signal pair rates as well as important noise terms, including spontaneous Raman generation. Using the rates determined for signal and noise photons, we calculate a coincidence-to-accidental ratio (CAR), which is a standard quantum system metric analogous to signal-to-noise ratio in classical signals. By increasing CAR, a quantum communications system will generate relatively fewer erroneous correlated measurement events. The calculation results for each of key source performance parameters are then later used as part of our system modeling, including projecting end-to-end throughput of a conceptual free-space QKD system.

The source model considered in our analysis is shown in Figure 3 below. We start with a simplified correlated photon pair source in order to focus the analysis on the most important materials-related properties, which have the greatest wavelength considerations. Additional passive components that would eventually be used for preparing complete hyperentangled states, including beam splitters, optical phase shifters, and delay line elements, are assumed to have relatively consistent loss across a broad spectrum of wavelengths, which can be justified by assuming one uses materials optimized for any particular wavelength of operation.
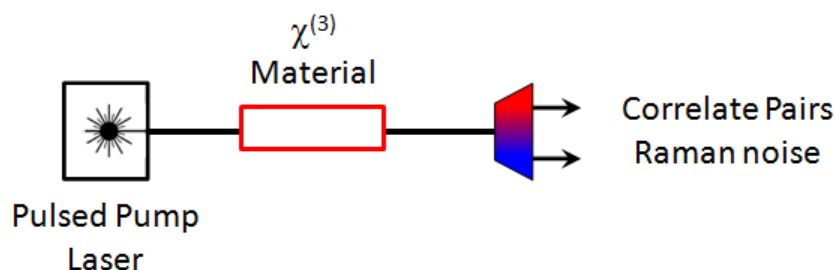


Figure 3. Source model for evaluating materials properties on correlated photon pair and Raman photon generation.

The materials identified for SFWM-based pair generation in each wavelength band are summarized in Table 1 below. The relevant materials properties, including the nonlinear refractive index ($n_2$) and Raman gain ($g_R$), have been taken from available literature. Where the exact wavelength variation of these parameters could not be found explicitly, established scaling rules were used to provide working estimates. It is important to note that each of these materials can all be fabricated into optical fibers in order to maximize the nonlinear interaction length. We assume that through proper waveguide design, the zero-dispersion wavelength can also be engineered for optimal correlated photon pair generation. For example, photonic crystal fiber (PCF) is assumed for pair generation at 0.8 μm in silica. Also, to simplify comparison, we assume the correlated photon pair filters are equally spaced from the pump (in terms of frequency) and as close as possible to the pump (within the practical constraints of filtering and pump suppression) for each wavelength band. In general, this tends to minimize the Raman noise and improve the coincidence-to-accidental ratio (CAR).

Table 1. Nonlinear SFWM Materials

| Wavelength (μm) | Materials |
|---|---|
| 0.8 | Silica PCF |
| 1.3 | Silica |
| 1.5 | Silica |
| 3.5 | Tellurite |
| 5 | $As_2S_3$ |
| 9 | $As_2Se_3$ |

Acronyms: SFWM = spontaneous four wave mixing; PCF = photonic crystal fiber

## 3.3 Quantum Channel: Modeling of the Free-Space Link

Once the hyperentangled pair has been generated at the transmitter, one of the photons is retained locally for half of the entanglement analysis, while the other photon is sent to the quantum receiver over the quantum channel. In the quantum communications system considered within this project, the quantum channel consists of a free-space link. We are assuming the quantum signal may propagate through a challenging maritime environment with widely variable atmospheric conditions including haze, fog, clouds, and rain, as well as scattering and turbulence effects. As described further in Section 3.5, we include in our system model additional sources of noise that can corrupt the quantum signal recovered at the receiver. One example is the noise introduced by environmental blackbody radiation which couples into the receive aperture.

The first channel impairment we considered through modeling is atmospheric propagation loss. SIT set up a MODTRAN simulation environment for atmospheric transmission modeling based on version 5.2.1 of the software. The atmosphere model selected in MODTRAN defines the temperature profile and ratio of major molecular gases assumed in the simulation, which include, for example, $H_2O$, $O_2$, CO, $CO_2$, and $N_2O$. For reference, the temperature profiles for different atmosphere models in MODTRAN are illustrated below in Figure 4 [6]. The U.S. standard atmospheric profile was used in our simulations.
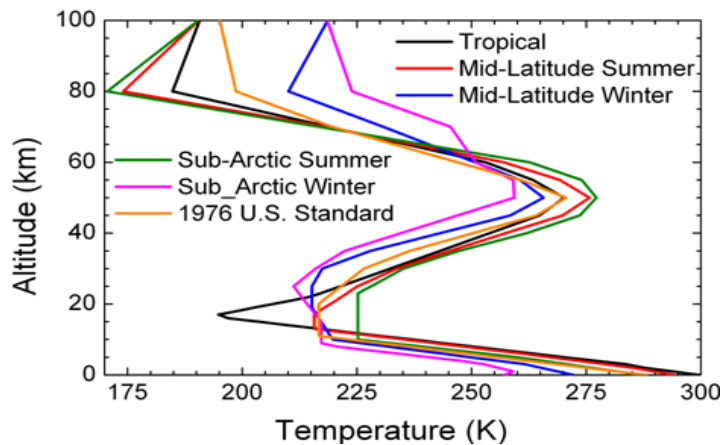


Figure 4. Temperature profiles for different atmosphere models in MODTRAN [6].

In addition to the absorption and scattering of molecular gases defined by the atmospheric profile, MODTRAN also includes the absorption and scattering of various aerosols in the atmosphere. Up to 5 different aerosol models were considered in the atmospheric transmission simulations, including (i) Navy Maritime, (ii) Maritime, (iii) Rural, (iv) Urban, and (v) Troposphere. As an example, the particle distribution for the Navy Aerosol Model is provided below in Figure 5 [7].
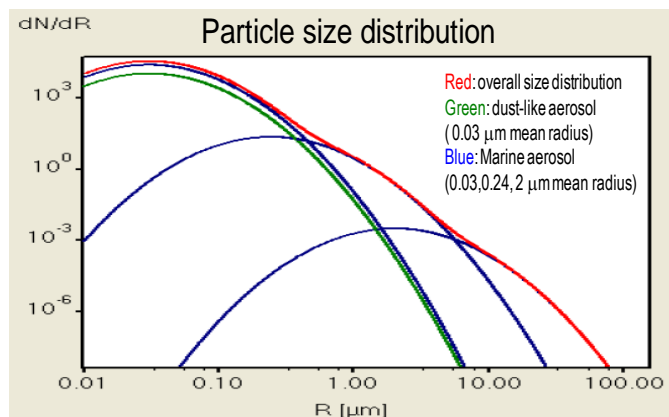


Figure 5. Particle size distribution for Navy Aerosol Model in MODTRAN [7].

MODTRAN simulations were performed over a 1-10 μm wavelength range (with 0.1, 1, 5, 15 cm$^{-1}$ resolution) assuming a 30 km free-space link distance at an altitude of 10 m. The effective visibility was varied from 5 km to 50 km by scaling the particle size distribution appropriately. Additional MODTRAN simulation parameters included a relative humidity of 50% and a wind speed=5 m/s. The results of modeling the free-space channel with the MODTRAN simulation tool are described later in Section 4.2.

In addition to our channel modeling effort, we began construction of an experimental testbed for characterizing the free-space wavelength-dependent loss through various simulated atmospheric conditions, which would be highly useful in validating theoretical models. This custom platform consists of a length of wide-diameter plastic tubing, which is coupled to a conventional alcohol-based fog machine. Various optical components are positioned at both tube openings for coupling a wide range of infrared wavelengths from NIR to LWIR in and out of the testbed. The system is designed so that variable levels of fog can be sustained in the tube in order to characterize their impact on optical transmissivity at each of the wavelengths of interest. The testbed is shown below in Figure 6. In Figure 6 (a), an oblique angle is used to show the entire setup. Also shown in Figure 6 are example configurations where the visible wavelengths transmissivity through the fog tube is varied from completely clear (b) to completely opaque (c).

In addition to the alcohol-based fog generator, we have also investigated alternative techniques capable of supporting a broader range of liquids, such as salt water, which would enable test conditions more closely simulating that of a harsh maritime environment. Our alternative fog generator is based on a commercial off-the-shelf piezo-based water mister. The manufacturer's data indicates that water droplets in the size range of 3-5 μm are produced by this device, which falls in the range of fog particles found in nature. We also note that particles of this size fall roughly in the center of one of the marine aerosol distributions shown in Figure 5. An example demonstration of the fog created by this generator is shown in Figure 6(d). Here, the water mister is simply placed into a pan of tap-water and turned on. A green laser pointer shows that observable scattering occurs in

this simulated fog. Future experiments could include, for example, adding impurities to the water, such as oceanic salt, to further vary the test conditions inside the fog chamber.
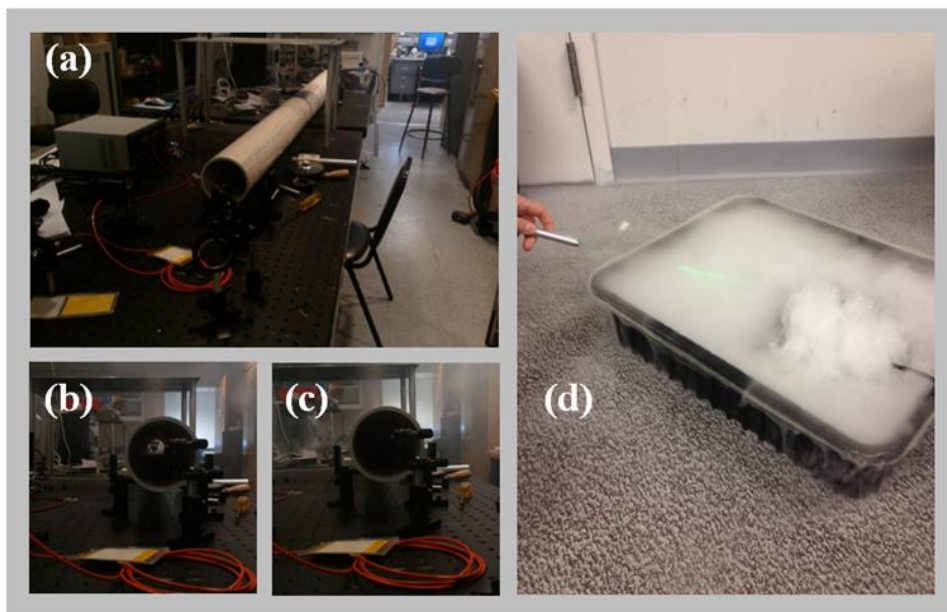


Figure 6. (a) The fog chamber for testing wavelength-dependent loss through various simulated atmospheric conditions. Also, examples of (b) high and (c) low transmissivity at visible wavelengths through the test chamber. (d) An alternative fog generation technique using a piezo water-mister.

## 3.4 Quantum Receiver: Modeling of Single-Photon Detector

After the hyperentangled photon propagates through the free-space quantum channel, it is recovered at the other end by the quantum receiver, as illustrated in Figure 1. The complete receiver includes elements for aligning the polarization reference frame to the transmitter, passive components for entanglement measurements in both time and polarization degrees of freedom, and the critical wavelength-sensitive element, which is the single-photon detector (SPD). We have focused our detector modeling efforts in this project on superconducting nanowire single-photon detectors (SNSPDs) due to their low dark count rates as well as high detection efficiencies (DE) and clock rates [8]. In addition, individual SNSPDs have been shown to work across a wide wavelength range, spanning from NIR to MIR [9], and SNSPDs are a potential solution for providing a single-platform technology for multi-wavelength-channel receivers. However, SNSPDs have not yet been demonstrated out to the 10 μm band, where as discussed in Section 4.2, there can be substantial improvements in the atmospheric transparency during adverse weather conditions, such as low visibility in the presence of fog. Given the very recent progress in SNSPDs, we consider two of the most promising material platforms, including niobium nitride (NbN) and tungsten silicide (WSi). We developed two different methods for projecting the performance of each of these SNSPD detectors for wavelengths out to 10 μm. The first extrapolation technique is based on fitting an empirical scaling law to the reported performance of NbN SNSPDs, while the second technique uses a more detailed device model that builds on recent developments in WSi detectors.

The empirical model incorporates NbN detector data that shows finite DE out to 5 μm, which was recently published by Marsili, *et al* [9]. The following empirical scaling law [10] was used for fitting to Marsili's data, allowing the detector's performance to be projected out to 10 μm:

$$\eta_{\det}(\lambda) = \frac{\eta_0}{1 + \left(\dfrac{\lambda}{\lambda_c}\right)^n} . \tag{1}$$

The parameters $\eta_0$ and $\lambda_c$ correspond to the efficiency limit at small wavelengths and the cut-off wavelength, respectively. The results of the fit to published experimental data along with our projections to longer infrared wavelengths are discussed in Section 4.3.

In addition to the advances in NbN-based SNSPDs, there has been very recent progress in new material platforms. In particular, recent results of detectors based on WSi promise greatly improved performance at longer wavelengths. In a recent demonstration reported by Marsili, *et al.* [11], the WSi SNSPDs are embedded in a resonant dielectric stack to provide significant enhancement to the DE beyond the single-pass absorption of the WSi film. Reported DE improves from ~20% to ~93% at 1.5 μm wavelengths. Using a detailed device model, we extended these results by projecting the performance out to longer MWIR and LWIR wavelengths.

In Marsili's WSi SNSPD device, the active superconducting detection material is amorphous Tungsten Silicide (WSi). As described in the supplementary material of [11], the authors report measurements on the material's complex refractive index. We have fit the wavelength dependence of the real and imaginary components of the complex refractive index, $n$ and $\kappa$, respectively, using the following linear expressions:

$$\begin{aligned} n &= 1.053 \cdot (\lambda - 1) + 4 \\ \kappa &= n - 1 \end{aligned} \tag{2}$$

where the wavelength, λ, is given in micron and the complex refractive index can then be written as $\tilde{n} = n - j\kappa$. Marsili graphically reports the measured complex refractive index from 1-2 μm. Yamada, *et al.*, [12] also report on the complex refractive index of WSi and show a linear dependence out to at least 10 μm. Therefore, in order to model the spectral characteristics of WSi, we were able to extend the useful range of Eq. (2) for the purposes of projecting WSi SNSPD performance out to 10 μm.

The SNSPD devices are WSi nanowire structures with widths and periods much smaller than the incident wavelength. An effective index for this sub-wavelength grating can be calculated based on the two adjacent materials, WSi and Si0$_2$, as well as their geometry. Anant, *et al.*, [13] provide the following equation for calculating the effective index of such a structure:

$$\tilde{n}_{eff} = \sqrt{(1-f) \cdot n_{SiO_2}^2 + f \cdot \tilde{n}_{WSi}^2} \tag{3}$$

where *f* is the spatial duty cycle of the grating. An effective imaginary component of the grating's refractive index can be computed as $\kappa_{eff} = -\mathrm{Im}(\tilde{n}_{eff})$. From the spectral dispersion of $\kappa_{eff}$, we can then calculate the wavelength dependence of the WSi-Si0$_2$ grating:

$$A(\lambda) = 1 - e^{-\frac{4\pi\kappa_{eff}L}{\lambda}}$$

(4)

where $L$ is the propagation length through the material. Using the fabrication details provided by Marsili [11], we assume 4.5 nm for the WSi thickness and 0.6 for $f$. The results are shown below in Figure 7. The trend observed in the computed absorption is in good agreement with modeling results presented elsewhere [14]. For simplicity, we have neglected the dispersion of silica in these calculations.
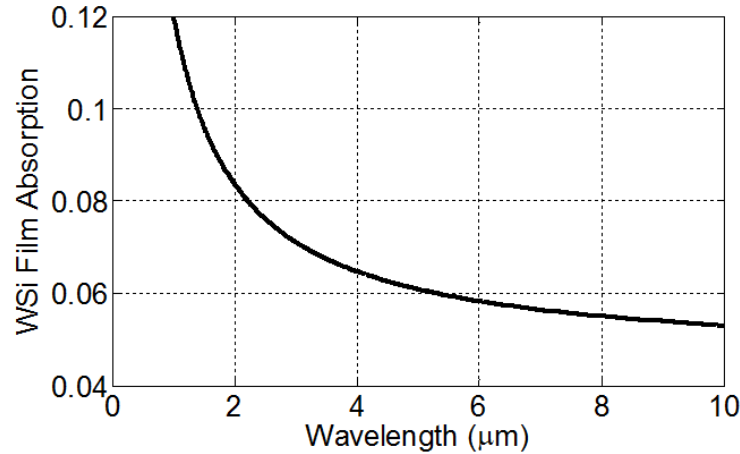


Figure 7. Modeled spectral dependence of single-pass absorption through amorphous WSi grating.

The results shown above in Figure 7 indicate the single-pass absorption through the sub-wavelength grating. One of the key advances reported by Marsili, *et al.*, is to embed this grating inside an optical resonator so that the incident single-photons have multiple opportunities to interact with the grating upon reflection within the cavity, which increases the overall probability of absorption and effective detection efficiency. This structure is shown below in Figure 8(a). The authors also provide modeling results for this structure [14], shown in Figure 8(b), which indicate a resonance peak near the target wavelength of 1.5 µm and a peak efficiency of almost 100%.
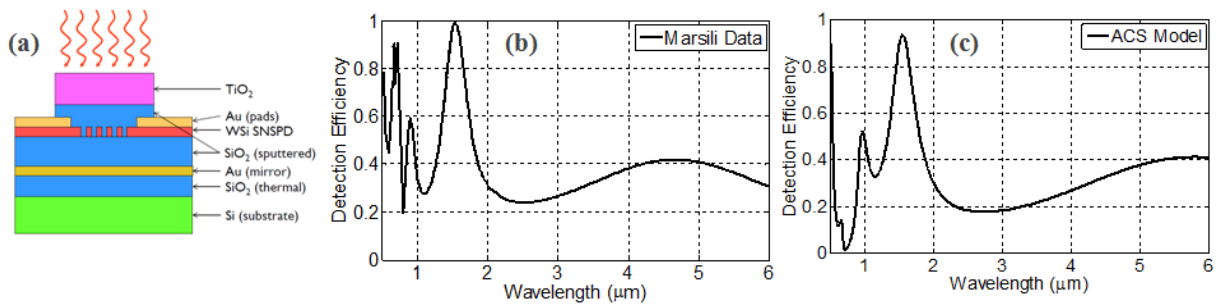


Figure 8. (a) The optical stack of WSi-based SNSPD reported by Marsili, et al [11, 14] for increased detection efficiency. (b) The modeled detection efficiency reported in [14] for the device structure shown in (a). (c) Computed detector efficiency using detailed device model developed as part of this effort.

We have developed our own detailed device model to describe the wavelength dependence of the structure shown in Figure 8. Our results are derived from transmission matrix theory [15], which

provides a powerful and flexible method for modeling multiple material layers. The device stack is built up from the following two matrices:

$$R_M = \frac{1}{t}\begin{bmatrix} 1 & r \\ r & 1 \end{bmatrix} \tag{5a}$$

$$P_M = \begin{bmatrix} e^{j\phi} & 0 \\ 0 & e^{-j\phi} \end{bmatrix} \tag{5b}$$

Eq. (5a) describes a reflection at an interface between two materials. The terms $r$ and $t$ are the complex field reflection and transmission coefficients, which are calculated from standard Fresnel equations, and $|r|^2 + |t|^2 = 1$. Eq. (5b) describes the propagation through a layer, where $\phi$ is the complex propagation constant describing both phase shift and attenuation. A matrix is constructed for each interface and layer, and all these elements are matrix-multiplied together to get the overall response of the device: $T = \prod_M R_M P_M$, where $T$ represents the device's complete transmission matrix. Once $T$ is determined, the device's scattering matrix ($S$) is calculated, from which the total optical power reflection ($|S_{11}|^2$) and transmission ($|S_{21}|^2$) parameters can be derived. From these $S$ parameters, the fractional power lost in the device can be calculated, which corresponds to the absorption in the WSi grating. Including the coupling efficiency from fiber to device ($\eta_c$) we derive the following expression for the DE:

$$\eta = \eta_c \left(1 - |S_{11}|^2 - |S_{21}|^2\right). \tag{6}$$

Using the device parameters provided by Marsili [11], including a 96.2% coupling efficiency, we use our MATLAB-based model to calculate the $S$ parameters in Eq. (6). The results of the simulation are shown above in Figure 8(c), and show good agreement with Marsili's modeling results, which are reproduced in Figure 8(b).

In order to project how well these latest developments in WSi nanowire detector technology might perform at much longer infrared wavelengths, we have adapted the multi-layer device structure, shown in Figure 8(a), to a simpler device model consisting of a structure with two end mirrors and a reflection-less layer of absorbing WSi-SiO$_2$ sub-wavelength grating material adjacent to a layer of SiO$_2$. We include only the material dispersion of the WSi while assuming the wavelength-dependencies of the other dielectrics could be compensated by tweaking the layer thicknesses or choosing other appropriate materials. In addition, this focuses the results on the impact of decreasing absorption by the WSi grating with increasing wavelength. This structure is also modeled using the matrix approach.
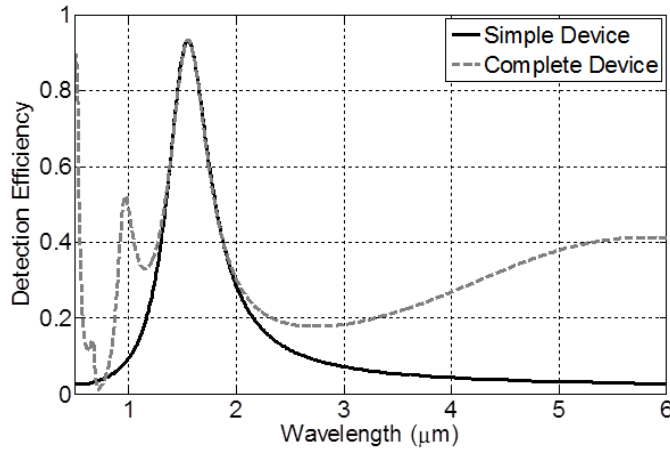
Figure 9. Comparison of the WSi-based SNSPD detection efficiencies for the detailed device model and the simplified device model.

Using the structure designed for 1.5 μm as a starting point, we optimize the simplified device model using the SiO$_2$ layer thickness, an arbitrary phase shift, and the front mirror reflectivity to produce a resonant peak closely overlapping with that of the detailed device model. The WSi grating parameters as well as the back mirror reflectivity are held constant. We observe excellent agreement in the 1.5 μm region between the two models as shown above in Figure 9. In Section 4.3 of this report, we discuss our modeling results as we re-optimize this WSi-based SNSPD structure for each of the longer MWIR and LWIR wavelength bands of interest at 3.5, 5, and 9 μm.

## 3.5  Quantum Communications: End-to-End System Modeling

We combine all three elements of the quantum communications system, including the quantum channel described in Section 3.2, the quantum channel discussed in Section 3.3, and the quantum receiver covered in Section 3.4 into an overall end-to-end system model.  The ultimate objective of our hyperentanglement QKD system modeling effort is to project its wavelength-dependent performance by including important system-level metrics such as estimates of key throughput.

In addition to the spontaneous Raman noise we mentioned as part of the transmitter discussion in Section 3.2, it is important to consider other potential sources of noise that can corrupt a quantum communications system.  For example, within the channel, in addition to the atmospheric loss considerations described in Section 3.3, the free-space beam can experience inhomogeneities and turbulence in the path that can result in time varying fluctuations of the received power at the single-mode receiver aperture [16].  Such effects have not yet been considered within the first year of this project.  However, another critical source of noise that was considered in this work is blackbody radiation, which results from the fact that the receiver aperture will effectively experience the background temperature of the incoming channel environment within its field of view. Given today's state-of-the-art superconducting nanowire detectors as described in Section 3.4, such blackbody radiation has been shown to effectively define the dark noise floor of the single-photon detection subsystem [11]. The single-mode photon probability of blackbody radiation is given by [17]

$$\mu_{BB} = \frac{\Delta \nu_{\text{det}} \Delta \tau_{\text{det}}}{\exp\left(h \nu_0 / k T_k\right) - 1}$$

where $\Delta\nu_{det}$ is the bandwidth of detection, $\Delta\tau_{det}$ is the detector gating window, $h$ is the Planck constant, $\nu_0$ is the center frequency, $k$ is the Boltzmann constant, and $T_k$ is the temperature in Kelvin.

Similar to the source metrics mentioned in Section 3.2, a coincidence-to-accidentals ratio ($CAR$) can also be calculated for the entire quantum communications system by considering valid entanglement coincidences after relevant system losses have been taken into account (i.e. channel transmittance, protocol efficiencies, excess component loss, and detector efficiency) compared to invalid coincidences that result from noise or other imperfections. In our system modeling, we assume spontaneous Raman scattering from the source and blackbody radiation as seen by detectors to be the dominant contributions to noise.

After the system CAR has been computed, the system two-photon visibility ($V$) is calculated using $V = (CAR-1)/(CAR+1)$ [19] and the quantum bit error rate ($QBER$) is calculated using $QBER = (1-V)/2$ [18]. Finally, using a entanglement-based system analysis modified from [19], the final key rate per detected pair is estimated by

$$R = q\big[1 - H_2(QBER + \xi) - f_{EC}(QBER)H_2(QBER)\big]$$

where $q$ is the basis reconciliation factor of ½, $H_2$ is the binary entropy function, $\xi$ is a security parameter, and $f_{EC}$ is an error correction efficiency parameter. Lastly, the rate, $R$, is scaled by the average detected coincidence per source pump pulse to estimate the final average key rate per pulse.

# 4    Results and Discussion

## 4.1  Quantum Transmitter: Source Architecture and Modeling

In this section, we discuss the results of our quantum transmitter modeling, the methods of which we described previously in Section 3.2. For reference, a more detailed drawing of the hyperentangled source architecture is provided in Figure 10.  The hyperentangled source consists of several subsystems, including the pulsed optical pump laser, the time-bin interferometer, and a polarization beam splitter combined with nonlinear fiber media in a loop to generate polarization entanglement. Making use of third-order fiber nonlinearity ($\chi^{(3)}$) and spontaneous four-wave-mixing (SFWM), single-photon pairs are generated non-deterministically in the nonlinear fiber with incoming pump pulses.  The architecture shown below is based on fiber-based components and interfaces, which has the advantage of maintaining photon pairs in a single spatial mode.  As mentioned previously, single-mode propagation through the atmosphere and receiver optics can offer advantages over multimode approaches. The use of $\chi^{(3)}$ material provides good compatibility with single-mode fiber, and the SFWM process for pair generation is relatively straightforward to demonstrate in practice.
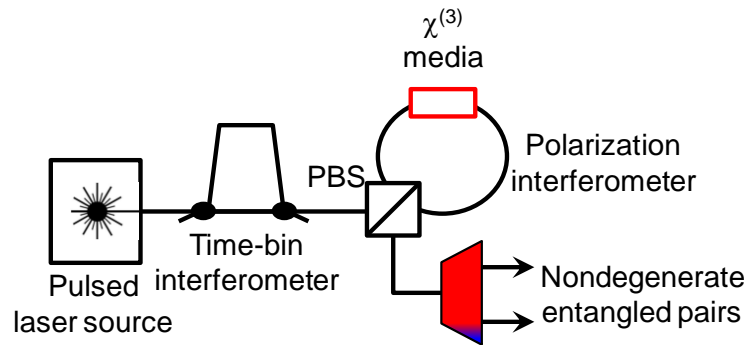


Figure 10. Source model architecture for generating hyperentangled photon pairs.  Sub-systems will be chosen and evaluated in terms of meeting the source metrics stated in the text.

Our efforts initially focused on identifying ideal optical pump sources, which will ultimately drive the nonlinearity which produces the single photon pairs.  We identified several critical parameters that must be satisfied by the pulsed optical pump so that the source can generate entangled pairs at sufficiently high rates for state-of-the art quantum communications.   These parameters are summarized below in Table 2 below and some reasoning behind each of the values is provided next.

Table 2. Pump Parameters

| Parameter | Value |
|---|---|
| Pulse Rate | 1 GHz |
| Time-bin Separation | <500 ps |
| Pulse FWHM | 10-100 ps |
| Peak Power | ~1 W |

A pulse rate of 1 GHz was chosen because we anticipate it can be reasonably matched with currently available gated single-photon detection technology.  However, depending on channel characteristics and detector efficiencies, higher pulse rates may be considered using more advanced detection

concepts. This pulse rate then dictates the requirements for the time-bin separation ($<$ ½ pulse period) and the pulse temporal full-width half-maximum (FWHM) so that there is no pulse field overlap at the output of the source. Finally, the pulse source must be capable of outputting sufficient peak powers to drive the nonlinearity to maintain sufficient mean pair numbers per pulse, $\mu$. A higher $\mu$ generally translates to higher key rates, although a limit of approximately 0.01 is typically assumed in entanglement-based QKD systems in order to minimize generation of more than a single photon pair, which could impact, for example, assumptions in the security model of the quantum communications system. In 1550 nm systems employing dispersion-shifted fiber, it is known that $\mu \propto (\gamma PL)^2$ [20] and $\gamma PL \sim 0.1$ is a reasonable estimate for typical implementations. Given the loss and nonlinear parameters of typical telecom optical fiber, for example, a pump peak power of ~1 W should be adequate for producing desired photon pair rates. This power level is used as a starting point for evaluating the various technological options currently available for optical pumps. Finally, our initial technology survey focused on self-pulsing sources, such as mode-locked lasers (MLL), due to low complexity and high peak powers that can be achieved. The output power of typical MLLs are sufficiently high that filtering to establish appropriate pulse widths and/or passive temporal multiplexing to GHz rates is feasible. The first step in establishing the system model is identifying technologies that are available in the wavelength bands of interest and are capable of meeting the pump source metrics outlined in Table 2. Our results are summarized below in Table 3. Many of these options are commercially available today, while others have been demonstrated or proposed in the literature and are likely to require additional technology development efforts.

Table 3. Pump Technologies

| Wavelength (µm) | MLL Options |
|---|---|
| 0.8 | Er+SHG, Ti:Sa |
| 1.3 | Pr, OPO |
| 1.5 | Er:glass |
| 3.5 | HoPr:ZBLAN |
| 9 | QCL, Er+DFG |

Acronyms: OPO = optical parametric oscillator, Er = erbium, SHG = second harmonic generation, Ti:Sa = titanium sapphire, Pr = praseodymium, Ho = holmium, ZBLAN = a family of fluoride glasses, QCL=quantum cascade laser, DFG=difference frequency generation.

Using the source model described previously in Section 3.1, the coincidence-to-accidental ratio (CAR) was calculated for each of the materials as a function of the pump power times the length (Power * Length = $PL$), as this product controls both the correlated photon pair and Raman noise generation rates. In our formulae, the former scales with the square of this product, and the latter is linearly proportional to the product.
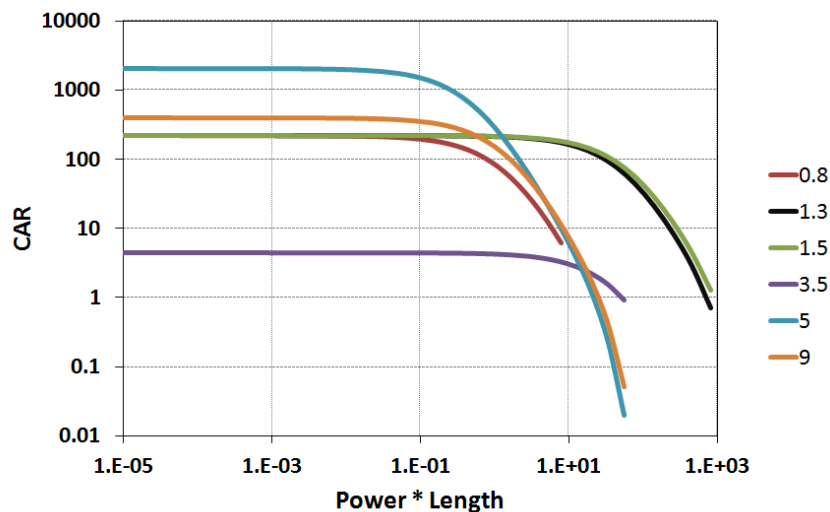
Figure 11. Calculated coincidence-to-accidental ratio (CAR) as a function of power*length for all wavelength bands

The results of the CAR calculation are summarized above in Figure 11. We observe that at low *PL*, the CAR approaches a large constant value for each material. In this regime, the relative quantity of the correlated pairs to noise photons is high; however, the pair generation rate is quite low. Silica fiber is a very common material for photon pair generation in the NIR and SWIR, and we observe that both of the chalcogenide fibers ($As_2S_3$ and $As_2Se_3$) in the MIR significantly out-perform silica in terms of CAR at low *PL*. As *PL* increases, the CAR tends to deteriorate, although the rapid decrease seen in each material occurs at different values of *PL*.
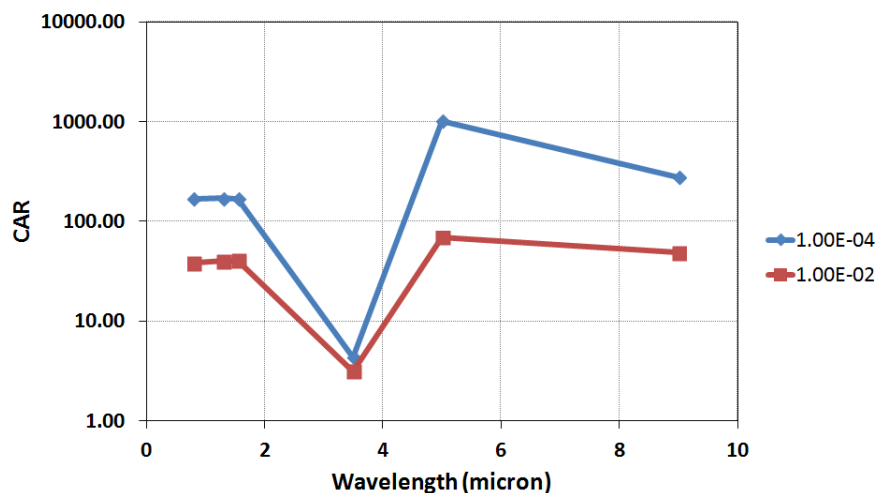


Figure 12. Calculated CAR in each wavelength band for two different mean photon numbers

Next, we computed the CAR in each wavelength band. The results are provided in Figure 12, where we have assumed constant correlated photon pair generation rates of $1x10^{-4}$ (blue) and $1x10^{-2}$ (red)). In this case, the *PL* product will be adjusted separately for each material in order to generate the desired pair rate. We note immediately that as the pair probability is increased by assuming a larger *PL*, the CAR is reduced, which is consistent with Figure 11. Generally, higher pair generation rates correspond to higher raw key rates for a QKD system; however, lower CAR leads to lower two-

photon visibilities and smaller effective key rates. Our modeling results in Figure 11 and Figure 12 suggest that the source *quality* is highest at the longer MIR wavelengths. However, since many other factors impact the overall quantum communications throughput, an entire system model is required to determine which wavelength band offers the best performance. The results of our end-to-end system modeling are provided in Section 4.3 of this report and incorporate the source model described here.

## 4.2  Quantum Channel: Modeling of the Free-Space Link

Using the MODTRAN simulation tool and configuration discussed earlier in Section 3.3, we present in this section our results of modeling the transmissivity of a 30 km free-space link. In Figure 13, the modeled transmissivity of this link, assuming a Navy Maritime aerosol model [1] and U.S. standard atmosphere is shown. Under reasonably high visibility conditions (e.g. 23 km, 50 km), relatively good transmittance windows can be observed in ~1.5-2 μm, ~2-2.5 μm, ~3.5-4 μm, ~5  μm, and ~8-10 μm wavelength regions. However, as visibility is reduced (e.g. 5, 10 km), the simulation results suggest significantly lower loss at longer wavelengths, with almost 5 orders of magnitude increase in the calculated transmittance at 10 μm vs. 1.5 μm when the visibility is only 5 km.

In order to explore the sensitivity of atmospheric transmission to different aerosol distributions, MODTRAN simulations were performed using a range of aerosol models including (i) Navy Maritime, (ii) Maritime, (iii) Rural, (iv) Urban, and (v) Troposphere. Simulations of both low visibility (e.g. 5 km) and higher visibility conditions (e.g. 23 km) were performed, and the results are shown in Figure 14. As in the Navy Maritime environment, there is a general trend towards reduced transmissivity, particularly at shorter wavelengths (e.g. 1 μm), when visibility is reduced.
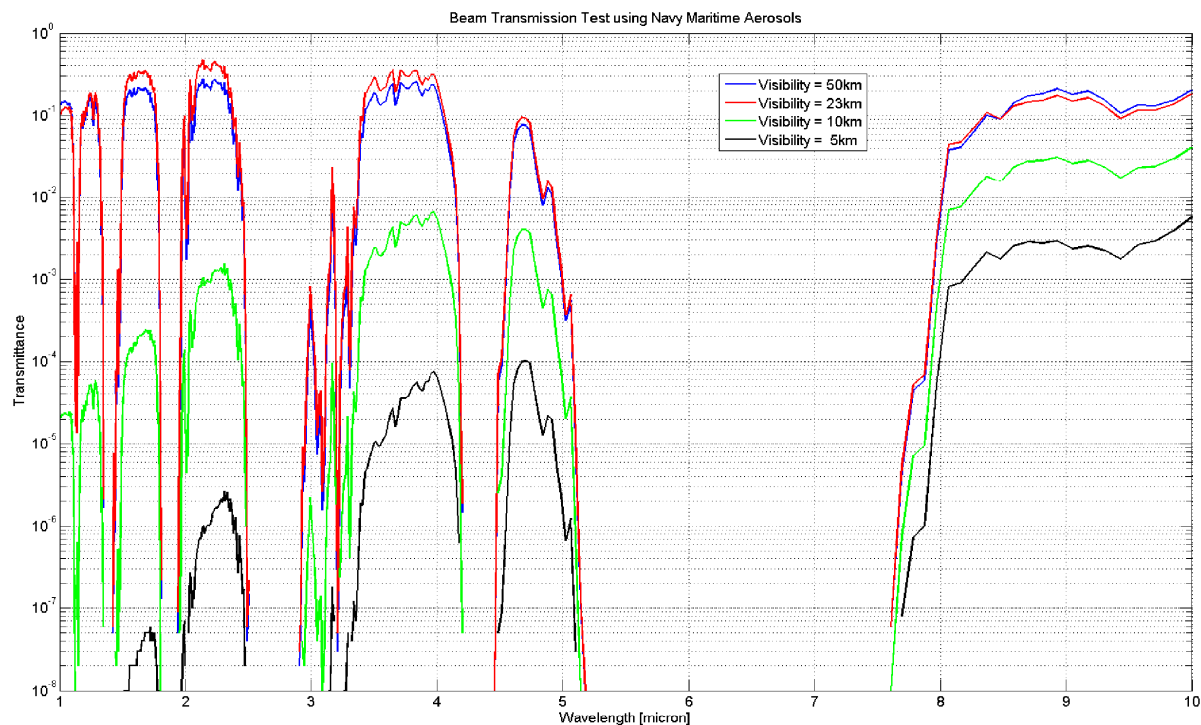
Figure 13.  MODTRAN atmospheric simulation of 30 km free-space link with different visibility levels.
(Navy Maritime aerosol model, U.S. standard atmosphere, additional simulation parameters defined in Section 3.3)
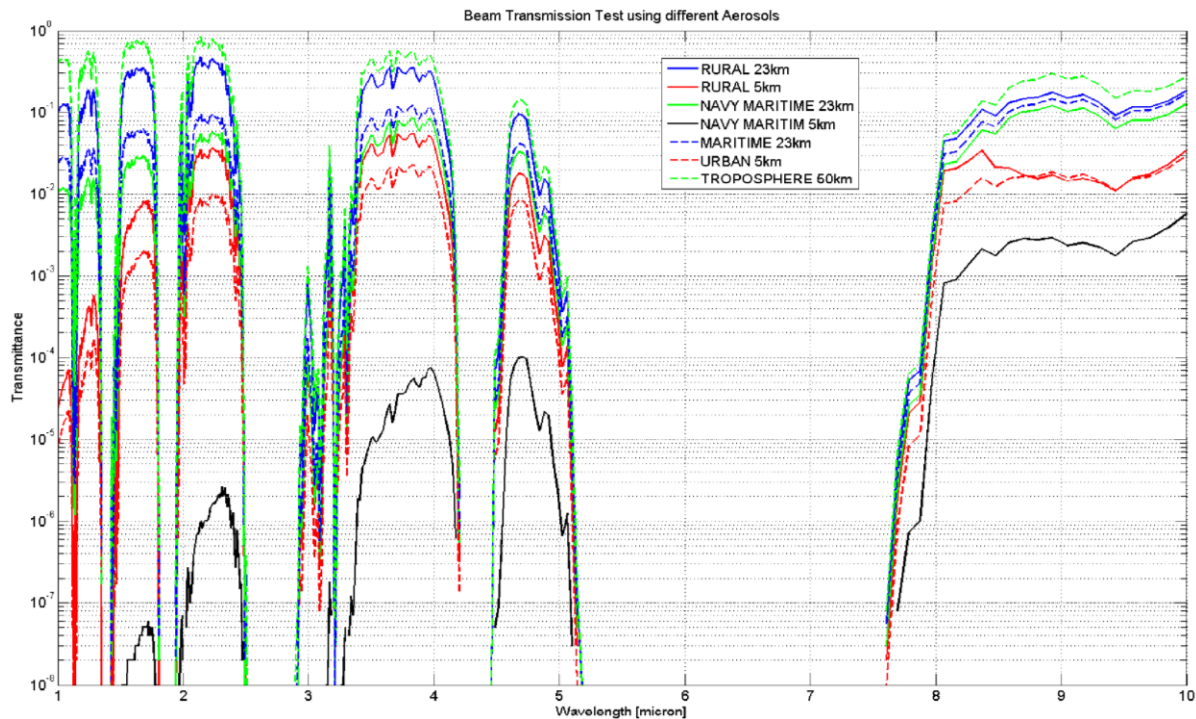
Figure 14. MODTRAN atmospheric simulation of 30 km free-space link with different visibility levels and different aerosol models. (U.S. standard atmosphere, additional simulation parameters defined in Section 3.3).

## 4.3 Quantum Receiver: Modeling of Single-Photon Detector

As described earlier in Section 3.4, our first method for predicting SNSPD performance for wavelengths out to 10 μm is to use the empirical model represented by Eq. (1) in order to extrapolate NbN detector data that has been reported to date [9]. The cut-off wavelength, $\lambda_c$, and the exponent, $n$, are used as fitting parameters to the experimental data. The results of this fit are provided in Figure 15 below. Since this particular device was not integrated within a resonant cavity, the detection efficiency was fairly low, even at shorter wavelengths (~1 μm), and its response rapidly rolls-off to less than 1% DE at 10 μm. Note that when considering the impact of such performance in a quantum communications link, the decreasing DE with increasing wavelength can ultimately counteract any potential gains in the channel transmissivity that might be seen at longer wavelengths under particular atmospheric conditions, such as discussed in the previous section.
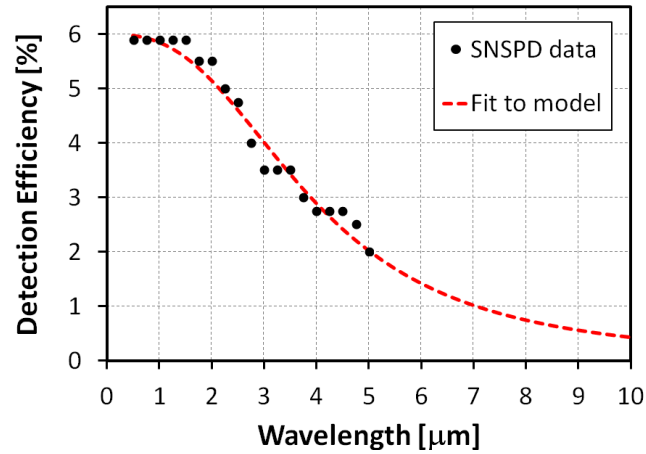
Figure 15. Projected NbN SNSPD efficiency vs. λ based on empirical model from [10] with fit to data from [9].

Our second method for projecting detection performance from NIR wavelengths to LWIR is based on recent advancements and demonstrations of WSi-based SNSPDs, which have gone beyond the performance demonstrated by NbN-based devices. In particular, the WSi resonant cavity-enhanced detector reported by Marsili, *et al*. [11] shows substantial improvement in DE over the NbN-based SNSPD results described in the last paragraph. However, we are not aware of a simple empirical scaling law which permits performance predictions of such resonant structures across the wide range of infrared wavelengths of interest. As a result, we developed the detailed resonant device model previously described in Section 3.4.   In this section, we present the results of our effort using this model to study the impact of the wavelength-dependent absorption of the WSi-Si0$_2$ grating layer on the SNSPD performance at various candidate wavelengths where reasonably good atmospheric propagation is likely to be expected.

As the absorption of the WSi grating decreases with wavelength (see Figure 7), we anticipate that the quality factor (Q-factor) of the optical cavity must be increased to achieve the same peak detection efficiency demonstrated, for example, at 1.5 μm.  The increased Q-factor of the resonator ensures a longer interaction time ($\tau_{det}$) between the incident photon and the WSi detection layer. However, increasing the interaction time can also slow down the response time of the detector, which must remain significantly less than the period at which successive entanglement measurements are made to ensure that there is no overlap between adjacent time slots. These two constraints can be summarized in the following inequality: $\tau_{\min} < \tau_{\det} < \tau_{clock}$, where $\tau_{min}$ is the minimum interaction time required to meet a threshold detection efficiency (DE) and $\tau_{clock}$ is the system clock period.  It is not obvious *a priori* whether or not this inequality can be satisfied by a resonantly-enhanced detector, but we explore this in our modeling effort as described below.

The simplified device model results for a 1.5 μm WSi-based detector are shown below (blue lines in Figure 16 (a)-(b)) on both wavelength and equivalent frequency scales. The blue curve shown on the wavelength scale is the same result shown earlier in Figure 9, which has a maximum DE of ~93% and fits well to the reported experimental results [11]. To re-optimize this simplified cavity for the other wavelength bands in the MWIR and LWIR (3.5, 5, and 9 μm), an internal phase shift, corresponding to an effective increase of the SiO$_2$ layer thickness, is applied to the cavity to

appropriately shift the resonance. The results from this modeling parameter adjustment are shown in Figure 16(a)-(b) (dash-dot lines) as DE versus both wavelength (a) and frequency (b). As expected, the peak DE decreases at the longer wavelength bands, consistent with the drop in absorption for the WSi detection layer.
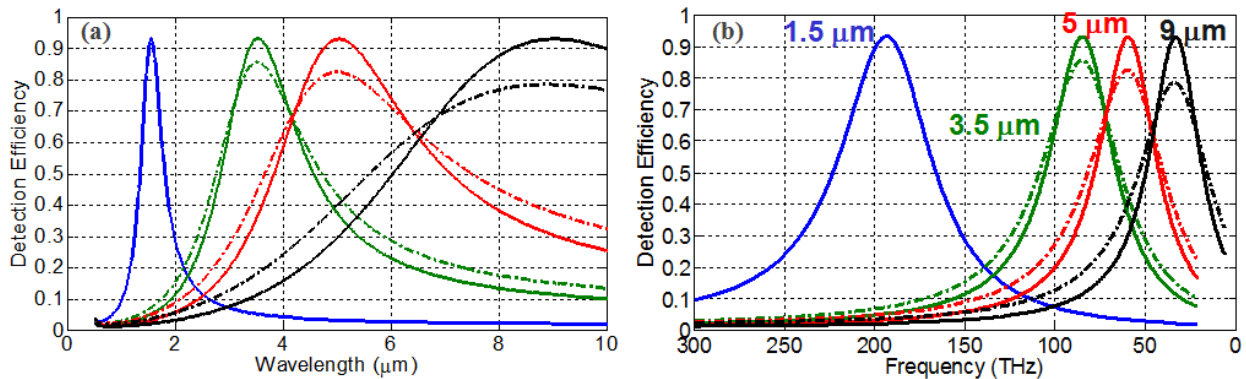


Figure 16. Projected detection efficiencies using simplified device model of 4 different WSi-based detectors optimized for the 1.5 (blue), 3.5 (green), 5 (red), and 9 (black) μm bands plotted versus wavelength (a) and frequency (b). Results are shown for both optimized (solid) and non-optimized (dash-dot) cavities.

This drop in DE can be compensated by increasing the reflectivity of the front facet of the cavity. This increases the cavity Q-factor and subsequently increases the detection efficiency and slightly reduces the detection bandwidth as shown by the solid lines. For each simplified detector model, the reflectivity is increased just to the point where the DE reaches the ~93% peak of the 1.5 μm WSi detector. While the bandwidth of detection decreases somewhat with increasing wavelength (this is most easily observed in Figure 16(b) where response is plotted on a frequency scale), its impact on a typical quantum communications system is likely to be minimal. For example, even at 9 μm, where the required increase in reflectivity is highest, the resulting bandwidth still exceeds 30 THz. With such large bandwidths, the response of the optical resonator should not place any additional constraints on the rate of the quantum transmitter or the quantum receiver, since modulation and detection timescales are typically on the order of ~ns, which would correspond to GHz-scale bandwidths. The results on WSi SNSPDs presented here suggest that resonant optical structures can be designed to enable very high DE out to MWIR and LWIR wavelengths while maintaining sufficiently fast response times for GHz-scale system clock rates.

## 4.4  Quantum Communications: End-to-End System Modeling

Building upon the individual results of the quantum transmitter, channel, and receiver analyses described in the recent sections, the end-to-end performance of the quantum communications system was computed using the system model described in Section 3.4. In particular, the two-photon entanglement visibility as observed by the system end points was projected at all of the source wavelengths of interest, including 0.8, 1.3, 1.5, 3.5, 5, and 9 μm. From this visibility, the final key rate per coincidence detection was estimated as well, as described in Section 3.4.

To gain an understanding of the impact of the atmospheric channel, two example visibility conditions were adopted from the MODTRAN simulation results presented earlier in Section 4.2. Using Figure 13 as a reference, these corresponded to a case of very good atmospheric visibility (23 km) and a case of moderate to good visibility (10 km). In addition to considering multiple channel

conditions, the impact of the different superconducting nanowire single-photon detector (SNSPD) models discussed in Section 4.3 on the quantum receiver performance was considered as well. The wavelength-dependant SNSPD models included (i) the empirical NbN model, which represents a fit to demonstrated NbN detector performance, (ii) the single-pass WSi model, which represents the projected performance of such detectors in absence of a resonant cavity, and (iii) the optimized WSi model, which is used to project performance of equivalent detectors in optimized cavity structures.
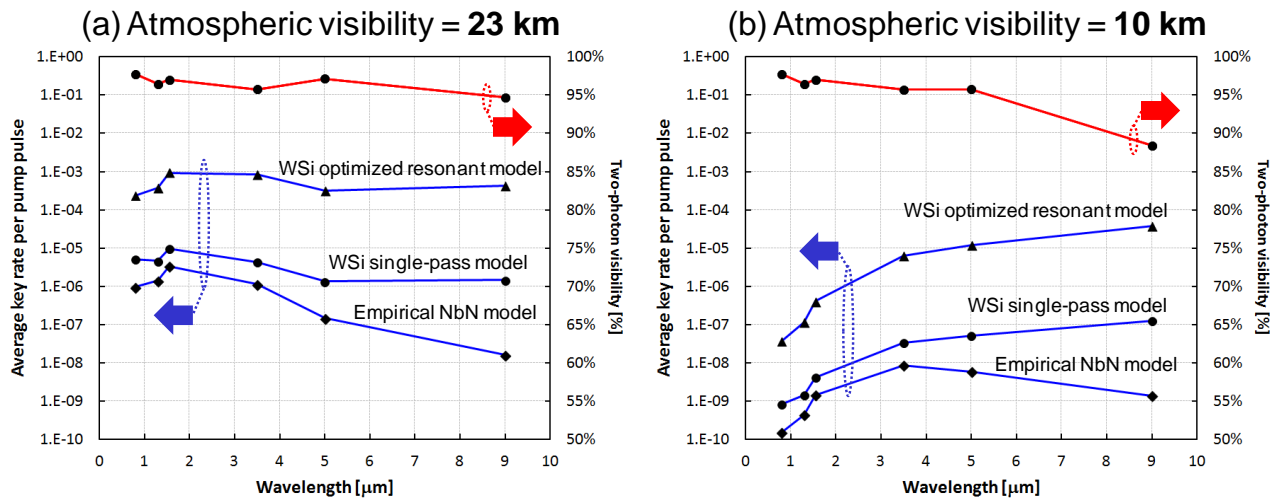


Figure 17. Modeling results of system two-photon visibility (*V*, right axis) and average key rate per pump pulse (left axis) as a function of wavelength at an atmospheric visibility of (a) 23 km and (b) 10 km. The system performance assuming three different models of SNSPDs (both NbN- and WSi-based) is projected from NIR (0.8 µm) to LWIR (9 µm) for each visibility condition.

The results of the end-to-end system modeling are provided in Figure 17(a) and (b). In the case of very good atmospheric visibility (e.g. 23km) and using the empirical NbN detector model, the projected key rates are highest near 1.5 µm SWIR band and continues to drop by more than two orders of magnitude as one moves towards MWIR and LWIR, as can be seen in Figure 17 (a). However, moving to a single-pass WSi detector, the performance variation from SWIR to LWIR is reduced to less than an order of magnitude, although the estimated performance remains highest near the 1.5 µm band. By moving to an optimized resonant WSi detector structure, the performance variation from SWIR to LWIR is reduced even further as can be seen in Figure 17 (a). This result suggests that by developing the appropriate components for the transmitter and receiver elements, quantum communications at LWIR transmission windows may approach that of current SWIR systems under the conditions of very good atmospheric visibility.

As seen in Figure 17 (b), the capability for operating at the longer infrared wavelengths becomes even more critical during less ideal atmospheric conditions, such as the 10 km visibility shown here. Even with state-of-the-art NbN detectors, the optimum throughput shifts from SWIR to a MWIR band of around 3.5 µm, as the empirical detector model results indicate. It is interesting that despite the fact that the modeled detection efficiency is reduced at these longer wavelengths as well as the fact that the source CAR is the lowest here, the improvements in channel loss more than compensate, resulting in a shift towards longer wavelength. Moving to the latest high-performance WSi detectors, the optimum shifts all the way to the LWIR, even assuming only a single-pass detector

model.  Finally, using an optimized resonant structure, the throughput estimates in Figure 17 (b) at 9 μm are now two orders of magnitude *greater* than that at 1.5 μm.

## 4.5  Deliverables/Milestones

| Date | Deliverable/Milestone | Status |
|:---:|:---:|:---:|
| June 2014 | Progress Report No. 1: Year 1, 1$^{st}$ Quarter | ✓ |
| August 2014 | Progress Report No. 2: Year 1, 2$^{nd}$ Quarter | ✓ |
| November 2014 | Progress Report No. 3: Year 1, 3$^{rd}$ Quarter | ✓ |
| January 2015 | Final Report | ✓ |

# 5   Conclusions

In this Final Report, we have summarized our 1-year effort on the Sea-optimized Quantum Key Exchange (SeaQuaKE) project, which has focused on assessing the critical wavelength-dependent performance considerations of a free-space maritime quantum communication system. The methods and results of analysis for the key subsystems, including quantum transmitter, quantum channel, and quantum receiver elements were described and combined into an end-to-end systems model. The system performance at a number of infrared transmission windows, ranging from near- to long-wavelength-infrared, was projected under different atmospheric conditions and different single-photon detector technologies. The results were used to highlight potential operating regions within this broad infrared spectrum where the highest performance of such systems might be achievable.

In terms of the quantum transmitter element, a hyperentanglement source architecture was developed that can be implemented at particular free-space transmission bands from 0.8 μm to 10 μm. Assuming state-of-the-art materials and components, the performance of the hyperentanglement source was projected across the various wavelength bands, providing estimates of pair generation capabilities at wavelengths which are inaccessible to current NIR and SWIR implementations. Despite relatively small variations in metrics, such as CAR, our analysis suggests that reasonably good source performance is likely to be achievable across each of the infrared bands of interest.

In terms of the quantum channel, MODTRAN simulations were conducted to assess the expected wavelength-dependent variations on free-space channel loss. Using the standard Navy Maritime aerosol model built into MODTRAN, results point to substantial benefits of operating in the longer infrared regions of MWIR and LWIR bands under low visibility conditions, which might occur, for example during periods of rain and fog [21].

As part of the quantum receiver, we provided wavelength-dependent detector models for multiple superconducting nanowire single-photon detector (SNSPDs) implementations. The modeling results suggest that through appropriate design and fabrication, major advances beyond the performance demonstrated in state-of-the-art NbN detectors, which currently have been optimized at SWIR, is possible at MWIR and even LWIR bands by realistic enhancements of WSi-based SNSPDs.

After combining all of the quantum communications subsystems into an end-to-end system model, our simulation results indicate that under very good visibility conditions with existing detectors, SWIR operation (e.g. 1.5 μm) is likely to provide the best performance. However, under less ideal atmospheric conditions, shifting to MWIR bands (e.g. 3.5 μm) can offer a performance advantage over SWIR operation even with existing detectors. Finally, with next-generation WSi SNSPDs optimized for resonant-enhancements, moving all the way to LWIR can offer even greater performance, and the impact when operating under good visibility is likely to be minimal compared to SWIR operation.

Our 1-year study focused on a number of critical wavelength considerations for a free-space quantum communications system, but additional factors have obviously not been included here and should be considered for future work. These include, for example, alternative source & detector technologies as well as more complex free-space channel effects, such as atmospheric turbulence [16] and variations in aerosol particle distributions [22].

# 6    References

[1] A. Berk *et al*., *MODTRAN 5.2.1 User's Manual*, Spectral Sciences Inc., Air Force Research Laboratory, USA, (2011).

[2] N. A. Peters *et al*., "Hyperentanglement and related technologies for quantum telecommunications," *SPIE DSS*, Paper 8727-1 (2013).

[3] T. Jennewein *et al*.," Quantum cryptography with entangled photons," Phys. Rev. Lett. 84, 4729–4732 (2000).

[4] W. Tittel *et al.*, "Quantum cryptography using entangled photons in energy-time bell states," Phys. Rev. Lett. 84, 4737–4740 (2000).

[5] Malik *et al*., "Influence of atmospheric turbulence on optical communications using orbital angular momentum for encoding," *Optics Express*, 20 (12), pg. 13195 (2012).

[6] MODTRAN FAQs, Retrieved from http://modtran5.com/faqs/index.html#model_atm (2014).

[7] A. M. J. van Eijk *et al*., "The Advanced Navy Aerosol Model (ANAM): validation of small-particle modes," *Proc. SPIE 8161*, p. 816108, 2011. doi:10.1117/12.896178.

[8] K. Berggren *et al*., "Detectors based on superconductors," in *Single-photon generation and detection, volume 45*, A. Migdall, S. Polyakov, J. Fan, J. Bienfang, eds. (Elsevier, 2013).

[9] Marsili *et al*., "Efficient single photon detection from 500 nanometer to 5 micron wavelength," *Nano Letters*, 12, pg. 4799 (2012).

[10] Engel *et al*., "Temperature-dependence of detection efficiency in NbN and TaN SNSPD" arXiv:1210.5395v1 [cond-mat.supr-con] (2012).

[11] F. Marsili et al., "Detecting single infrared photons with 93% system efficiency," *Nat. Photonics* 7(3), 210–214 (2013).

[12] Yamanda *et al.*, "Mid-infrared wire-grid polarizer with silicides," *Optics Letters*, 33 (3), pg 258 (2008).

[13] Anant *et al.*, "Optical properties of superconducting nanowire single-photon detectors," *Optics Express*, 16 (14), pg. 10750 (2008).

[14] F. Marsili *et al.*, "Mid-infrared single-photon detection with tungsten silicide superconducting nanowires," *CLEO 2013* presentation slides, paper CTu1H.1 (2013).

[15] L. A. Coldren and S.W. Corzine, *Diode Lasers and Photonic Integrated Circuits*, Chap 3, (Wiley & Sons, 1995).

[16] L. C. Andrews and R. L. Phillips, *Laser Beam Propagation through Random Media*, (SPIE Press 2005).

[17] Temporao *et al*., "Feasibility study of free-space quantum key distribution in the mid-infrared," *Quantum Information and Computation*, 8, pg. 0001 (2008).

[18] N. Gisin *et al*., "Quantum cryptography," *Rev. Mod. Phys.* 4, 41.1-41.8 (2002).

[19] J.-P. Bourgoin *et al*., "A comprehensive design and performance analysis of low Earth orbit satellite quantum communication," *New J. Phys.* 15, 023006 (2013).

[20] S. D. Dyer, M. J. Stevens, B. Baek, and S. W. Nam, "High-efficiency, ultra low-noise all-fiber photon-pair source," *Opt. Express* 16(13), 9966–9977 (2008).

[21] R. Martini *et al.*, "Free-space optical transmission of multimedia satellite data streams using mid-infrared quantum cascade lasers," *Electron. Lett.* 38, pp. 181-183 (2002).

[22] C. N. Reinhardt *et al.*, "A reconsideration of the best wavelengths for free-space optics," *Proc. SPIE 9224, Laser Communication and Propagation through the Atmosphere and Oceans III,* 92240Q (2014).